Chemical Engineering Journal 427 (2022) 131712

Contents lists available at ScienceDirect

Chemical Engineering Journal

journal homepage: www.elsevier.com/locate/cej

In-situ synthesis of microflower composed of N-doped carbon films and Mo_2C coupled with Ni or FeNi alloy for water splitting

Feifei Peng [a], Luhong Zhang [a], Bin Jiang [a], Haozhen Dou [b], Mi Xu [a], Na Yang [a], Jiazhu Zhang [a], Yongli Sun [a,*]

[a] School of Chemical Engineering and Technology, Tianjin University, Tianjin 300072, China
[b] Department of Chemical Engineering, University of Waterloo, Waterloo, Ontario N2L 3G1, Canada

ARTICLE INFO

Keywords:
Molybdenum carbide
Water splitting
Nickel–iron alloy
Flowerlike
Nitrogen-doped carbon

ABSTRACT

Water electrolysis represents a promising technology for the production of hydrogen fuels. High-performance and stable non-noble electrocatalysts for hydrogen evolution reaction (HER) and oxygen evolution reaction (OER) are urgently desired to improve the efficiency of water splitting for large-scale hydrogen production. Herein, a flowerlike heterojunction catalyst composed of N-doped carbon films and Mo_2C nanoparticles strongly coupled with ultrasmall Ni or FeNi alloy (Ni-Mo_2C/CF or FeNi-Mo_2C/CF) is in-situ synthesized for efficient water splitting. The as-prepared samples with unique architecture and composition combine the synergistic effects of both geometric design and electronic modification, possessing plenty of active sites, robust heterostructures, abundant channels for rapid mass transport and electron/ion transfer, and the improved conductivity for high-efficiency charge exchange during electrocatalytic process. The optimized Ni-Mo_2C/CF for HER and FeNi-Mo_2C/CF for OER achieve overpotentials of 81 and 228 mV to reach 10 mA cm^{-2}, respectively, in 1.0 M KOH. Furthermore, the FeNi-Mo_2C/$CF^{(+)}$//Ni-Mo_2C/$CF^{(-)}$ alkaline water electrolyzer demonstrates a low cell voltage of 1.53 V at 10 mA cm^{-2}, outperforming most ever-reported water electrolyzer cells, and impressive stability over 24 h at 50 mA cm^{-2}. This work provides a facile and effective method to construct high-performance and non-precious metal electrocatalysts for commercial water splitting.

1. Introduction

As a renewable and high-efficient source, hydrogen accompanied with the features of high energy density and carbon-free energy carrier has been expected to play a critical role in the future sustainable energy [1,2]. Electrochemical water splitting for hydrogen production, which offers an attractive route to the storage of renewable but intermittent energy, is one of the currently ongoing frontiers [3,4]. The process involves two half reactions: one is the Hydrogen evolution reaction (HER) at cathode electrode and the other is Oxygen evolution reaction (OER) at anode electrode [5,6]. The efficiency of water electrolysis is limited by the high kinetic overpotential associated with sluggish kinetics resulting from HER with water adsorption and dissociation to H adsorbed (H_{ads}) at the Volmer step and OER with complicated four-electron transfer process ($4OH^- \rightarrow O_2 + 2H_2O + 4e^-$), respectively, in alkaline solution [7–9]. Therefore, developing highly efficient electrocatalysts is critical for facilitating fast kinetics. The Pt-based and RuO_2-/IrO_2-based materials are regarded as benchmark of HER and OER catalysts respectively [10,11]. However, their limited storage and high cost largely restrict their practical applications. Hence, efficient and durable non-precious electrocatalysts are highly desired.

Recently, non-noble transition-metal carbides have received extensive research interest as catalysts for the electrochemical water splitting. Among them, molybdenum carbides have attracted ample attention as active materials especially for the efficient HER in both acidic and basic solutions as a result of its d-band electronic structure to Pt-group metals [12,13]. Enormous attempts have been made to improved catalytic performance of Mo_2C, such as constructing various morphologies and synthesizing different crystal phases [14–16]. Additionally, Mo_2C integrated with N-doped carbon as supporter can prohibit its serious sintering during preparation at extremely high temperature and suppress its aggregation/corrosion during electrocatalytic process. Meanwhile, the N-dopant was able to further improve the performance of the whole catalyst [17]. Nevertheless, the electrochemical properties of pure Mo_2C

* Corresponding author.
E-mail address: sunyongli@tju.edu.cn (Y. Sun).

https://doi.org/10.1016/j.cej.2021.131712
Received 4 May 2021; Received in revised form 29 July 2021; Accepted 3 August 2021
Available online 25 August 2021

are far from those of Pt-based metals. The strong adsorption of H on Mo_2C surface prohibit the desorption of H_{ads} to generate H_2 resulting in its lower performance [18,19]. Hence, accommodating the electronic structure of Mo such as designing heterogeneous of Mo_2C and 3d transition metals to accelerate the desorption of H_{ads} is an effective strategy to decrease the overpotential of HER [20]. Nickel doped Mo_2C has been proved to be able to reduce the empty d-orbit of Mo by donating electron to Mo, which could weaken the energy of Mo–H bonds to moderate the adsorption/desorption of H_{ads} [21,22]. Furthermore, the surface $Ni^{2+\delta}$ ($0 \leq \delta \leq 1.5$) is propitious to facilitate water dissociation during HER in alkaline electrolyte [23]. Although the heterogeneous catalysts of Ni and Mo_2C have exhibited better HER properties than bare Mo_2C, it is convinced that constructing novel Ni-Mo_2C based materials with abundant active interfaces between Ni and Mo_2C can enhance their interaction and further considerably improve the electrocatalytic performance toward HER. Accordingly, decreasing the size of Ni as well as Mo_2C and introducing nitrogen-doped carbon materials as the supporter of Ni-Mo_2C can fabricate numerous active heterointerfaces and enhance the synergistic effect among the three species, which are expected to endow the catalyst with outstanding electrocatalytic activity and stability for HER.

Recently, some studies have shown that Mo_2C doped with Ni as bifunctional catalyst exhibited low overpotential during overall water splitting. For instance, Lu and Li et al. fabricated Ni coupled with Mo_2C encapsulated in nitrogen-doped carbon nanofibers for overall water splitting, achieving a current density of 10 mA cm^{-2} at a voltage of 1.64 V [23]. Yu and co-workers synthesized the porous carbon-supported Ni-Mo_2C as the bifunctional catalyst for water splitting, showing a voltage of 1.66 V at 10 mA cm^{-2} [24]. Whereas its catalytic activity and stability for OER should be further improved to fulfill practical applications. Particularly, FeNi-based catalysts delivered a considerable enhanced OER activity than single Ni-based catalysts according to many reports [3,25,26]. Recently, several effective strategies have been developed to further enhance the OER activity of NiFe-based electrocatalysts, including optimizing the Ni/Fe composition, designing different morphologies and tuning the phases [27–29]. Nevertheless, further research shows that the metal on the surface of the catalysts will undergo superficial or complete reconstruction into metal (oxy)hydroxides during water oxidation in alkaline solution, revealing that the (oxy)hydroxides formed in-situ are veritable active species for OER [30,31]. In general, metal (oxy)hydroxides exhibit intrinsically low conductivity, which hinders the electron transfer and impedes the efficiency of OER [32,33]. Metal (oxy)hydroxides integrated with conductive substrate to construct OER catalysts is an effective strategy to enhance the efficiency of electron transfer during the catalytic process. Ideally, the conductive substrate should possesses multimodal pore size distribution with interconnected micropores (<2 nm), mesopores (2–50 nm), and macropores (greater than50 nm) to adequately expose the active sites and funnel the reactants and electrolytes into the active sites. However, the mostly reported substrates to date are Ni foam or carbon cloth with large holes rather than multimodal pores [34]. Meanwhile, decreasing the lateral size and vertical thickness of the metal oxides/oxyhydroxides enables the reduction of the transport resistance of electrons from the surface catalyst to the electrode, which is also an effective strategy to improve the charge transfer efficiency for OER but still quite challenging [35]. Accordingly, ultrafine FeNi oxyhydroxides, immobilized on a conductive supporter with trimodal-porous structure, are expected to adequately expose the active sites, facilitate the mass transport, and significantly improve the charge transfer efficiency during the OER. Furthermore, the same strategy to synthesize electrocatalysts with abundant intrinsic active sites as well as good durability for both HER and OER is also a challenge.

Herein, we report a scalable strategy to in-situ synthesize a flower-like heterojunction catalyst composed of N-doped carbon films and Mo_2C nanoparticles strongly coupled with ultrasmall Ni or FeNi alloy for electrocatalytic water splitting. With the unique trimodal-porous structure, microsize dimension, and composition, the as-prepared samples incorporate the synergistic effects of both geometric design and electronic modification, which are significant for the improved activity. The content of Ni in Ni-Mo_2C/CF has been optimized to achieve a low overpotential of 81 mV to reach 10 mA cm^{-2} with a small Tafel slope of 43.5 mV dec^{-1} toward HER in 1.0 M KOH, demonstrating a much better HER activity than Mo_2C/CF (138 mV, 57.6 mV dec^{-1}) and an attractive stability. More importantly, the optimized Ni-Mo_2C/CF requires lower overpotential than the commercial Pt/C to obtain a current density larger than 93 mA cm^{-2}. The OER performance of FeNi-Mo_2C/CF has been also optimized by tuning the mole ratio of Fe to Ni. The optimized catalyst exhibits a much better performance of OER than the commercial RuO_2 and only requires the overpotential of 228 mV to obtain 10 mA cm^{-2} in 1.0 M KOH, and shows a satisfactory stable activity. Significantly, the FeNi-Mo_2C/$CF^{(+)}$//Ni-Mo_2C/$CF^{(-)}$ alkaline water electrolyzer demonstrates a low cell voltage of 1.53 V at 10 mA cm^{-2}, superior to the $RuO_2{}^{(+)}$//$Pt/C^{(-)}$ couples (1.556 V) and most of previously reported remarkable full-cells for overall water splitting.

2. Results and discussion

2.1. Preparation and material characterizations

The synthetic route for FeNi-Mo_2C/CF is presented in Fig. 1. Firstly, hollow Mo-precursor microflowers (Mo-PMI_n) were prepared through a hydrothermal method [12]. Subsequently, the solution of $K_2Ni(CN)_4$ and $K_3Fe(CN)_6$ was introduced to the mixture of PMI_n/Mo-PMI_n, which led to the fabrication of hollow FeNi-PMI_n/Mo-PMI_n microflowers. Finally, the hollow FeNi-Mo_2C/CF microflower was obtained by the calcination of FeNi-PMI_n/Mo-PMI_n at 700 °C under an Ar atmosphere. Particularly, they displayed two distinctly different colors (Fig. S1), suggesting different compositions in them. Additionally, the hollow flowerlike Ni-Mo_2C/CF was synthesized in parallel by the same method as that for FeNi-Mo_2C/CF except for no addition of $K_2Ni(CN)_4$. For comparison, M(M = Fe, Co, FeCo)-Mo_2C/CF and Fe-//Ni-Mo_2C/CF (mechanically mixing Fe-Mo_2C/CF and Ni-Mo_2C/CF with mole ratio of 0.7) were also prepared. Different contents of metallic Ni were prepared by adjusting the addition amount of $K_2Ni(CN)_4$. The mole ratios of Fe to Ni in FeNi-Mo_2C were tuned by adding different proportions of $K_2Ni(CN)_4$ and $K_3Fe(CN)_6$. The synthesis details are summarized in Table S1 (Supporting Information). The contents of Fe and Ni in catalysts were determined by inductively coupled plasma mass spectrometry (ICP-MS) (Table S2). Based on the mole ratios of Fe to Ni in FeNi-Mo_2C/CF, the samples were labeled as *x* FeNi-Mo_2C/CF, where *x* is the value of the mole ratio of Fe to Ni. Besides, based on the content of Ni in FeNi-Mo_2C/CF, the samples were marked as *x*% Ni-Mo_2C/CF, where *x*% represents the mass fraction of Ni in Ni-Mo_2C/CF. In the figures of this article, Ni-Mo_2C/CF and FeNi-Mo_2C/CF stand for 5.8% Ni-Mo_2C/CF and 0.7 FeNi-Mo_2C/CF, respectively, unless otherwise specified.

Then, X-ray diffraction (XRD) analysis was employed to determine the crystal structure of as-prepared samples. As shown in Fig. 2a, X-ray diffraction (XRD) patterns indicate that all of the samples are composed of β-Mo_2C (PDF#35-0787) [36] and the corresponding metal or alloy. Notably, the peaks of Mo_2C doped by metal or alloy migrate to a higher angle compared to that of bare Mo_2C/CF (Fig. S2), indicating metal atoms inserting into the β-Mo_2C crystal structure during the pyrolysis process, resulting in shrinkage of Mo_2C unit cell volume. Besides, as depicted in Fig. S3, the diffraction peak of metallic Ni in Ni-Mo_2C/CF shifts to a lower angle (from 44.5° to 44.3°) in comparison to bare Ni (PDF#04-0850), revealing the strong interactions between Ni and Mo_2C components. In addition, with the increase of Ni content, the intensity of diffraction peak of metallic Ni in Ni-Mo_2C/CF increases gradually. As illustrated in Fig. S4, the FeNi-Mo_2C/CF has similar diffraction peaks to those of Ni-Mo_2C/CF while the peak of metal shifts slightly to a lower angle (from 44.3° to 44.0°), such a peak shift might be attributed to the lattice expansion because the larger Fe atoms replace the smaller Ni

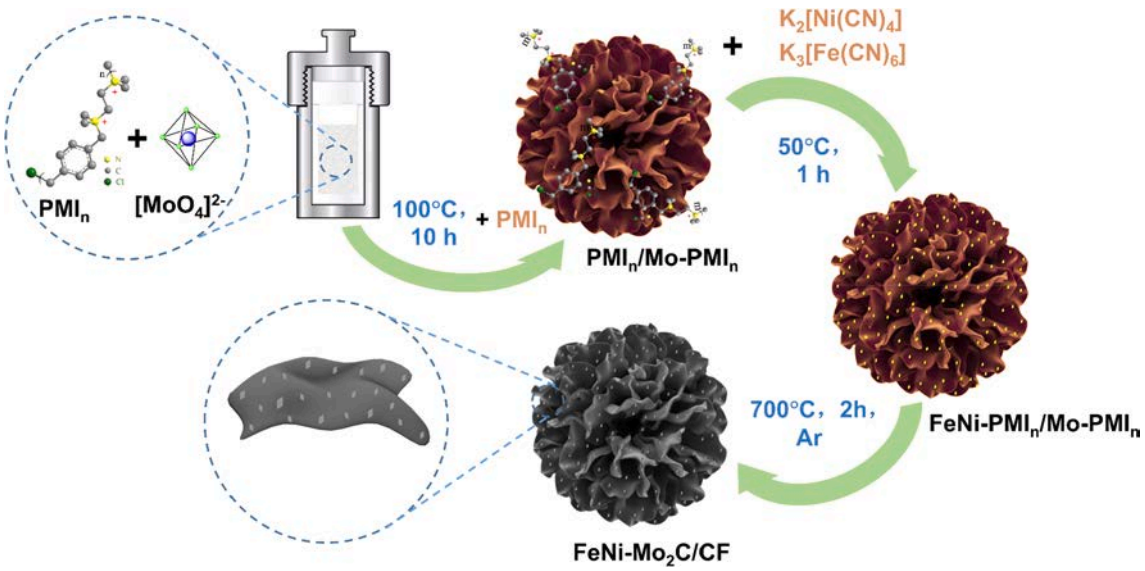

Fig. 1. Schematic of the synthesis of the FeNi-Mo$_2$C/CF.

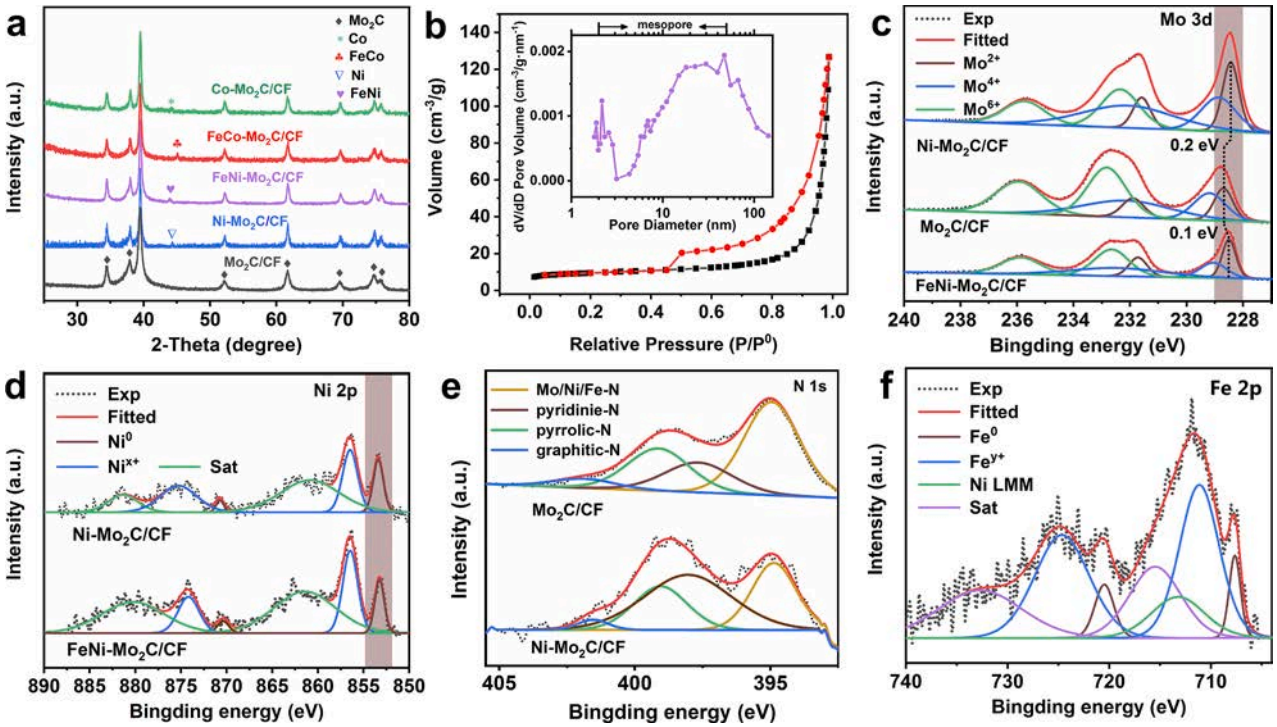

Fig. 2. (a) XRD patterns of different catalysts. (b) N_2 adsorption–desorption isotherm of FeNi-Mo$_2$C/CF, Inset: the corresponding pore-size distribution. (c) XPS spectra of Mo 3d in Ni-Mo$_2$C/CF, Mo$_2$C/CF, and FeNi-Mo$_2$C/CF. (d) XPS spectra of Ni 2p in Ni-Mo$_2$C/CF and FeNi-Mo$_2$C/CF. (e) XPS spectra of N 1s in Mo$_2$C/CF and Ni-Mo$_2$C/CF. (f) XPS spectra of Fe 2p in FeNi-Mo$_2$C/CF.

atoms, and no other diffraction peaks from bare Fe or metal oxide/hydroxide can be observed, indicating that Fe atoms are successfully incorporated into nickel atoms to form FeNi bimetallic alloy. Moreover, with the increase of Fe content, the diffraction peak of FeNi alloy shifts toward lower diffraction degrees (from 44.0° to 43.8°), and the diffraction peak of FeNi alloy in FeNi-Mo$_2$C/CF is broader than that of Ni in Ni-Mo$_2$C/CF, which may be due to the distortion of the lattice. The pore structure characteristics of FeNi-Mo$_2$C/CF were analyzed by N_2 adsorption–desorption isotherms (Fig. 2b), confirming its unique trimodal-porous structure with macro-, meso-, and micropores. X-ray photoelectron spectroscopy (XPS) was conducted to further investigate the chemical composition and valence state of the catalyst surface. As shown in Fig. S5a, the XPS full spectrums of the samples reveal the co-existence elements on their surfaces, and the results correspond with the phase in the samples determined by XRD. In the high-resolution spectroscopy, Fig. 2c displays the Mo 3d XPS spectra of Ni-Mo$_2$C/CF, Mo$_2$C/CF, and FeNi-Mo$_2$C/CF, exhibiting Mo^{2+}, Mo^{4+}, and Mo^{6+} species on the surface [37]. The Mo^{4+} and Mo^{6+} species should originate from the oxidation of the Mo$_2$C when exposed to air [38]. Specifically, the characteristic doublet Mo^{2+} peaks for Ni-Mo$_2$C/CF and FeNi-Mo$_2$C/CF are negatively shifted by 0.1 and 0.2 eV with respect to those of Mo$_2$C/CF, respectively. Similarly, the peaks of Mo^{4+} and Mo^{6+} also shift to a

lower binding energy, suggesting lower valence of the Mo species. It is worth highlighting that, the proportions of Mo^{2+} species on both Ni-Mo_2C/CF and FeNi-Mo_2C/CF surface increase, which could due to the electrons transfer from Ni and FeNi to Mo_2C, respectively, or the inhibited oxidation of Mo_2C by the defense of Ni and FeNi alloy. In the high-resolution Ni spectrum of Ni-Mo_2C/CF (Fig. 2d), the peaks at 856.5 eV and 874.2 eV can be assigned to the Ni^{x+} $2p_{1/2}$ and Ni^{x+} $2p_{3/2}$, respectively, which are probably associated with the Ni—N_x or Ni—O bond on the surface of Ni nanoparticles [11]. The peaks located at 853.2/870.4 eV are ascribed to metallic Ni (Ni^0), and the existence of metallic Ni in Ni-Mo_2C/CF is well consistent with XRD analysis. Notably, the peaks of Ni^0 in Ni-Mo_2C are positively shifted by around 1.0 eV as compared to those of the Ni^0 (852.2/869.3 eV) in bare Ni based materials reported by some researchers [23,39]. In general, a reduction in binding energy results from an increase of the valence electron charge. On the basis of these views, the distinct binding energy shifts for Ni-Mo_2C/CF should be attributed to the transfer of valence electrons from Ni to Mo_2C via the abundant phase interfaces between Ni and Mo_2C, which leads to the lower Mo valence state and the higher Ni valence state. As well known, the surface electronic configuration of the catalysts has a remarkable effect on the catalytic activity [40]. This efficient electron transfer in Ni-Mo_2C/CF contributes to a synergistic effect between Ni and Mo_2C, diminishes the hydrogen binding energy during HER, and thereby promotes the desorption of H_{ads} and H_2 generation. Moreover, the presence of metallic Ni can improve the electronic conductivity of Ni-Mo_2C/CF, which is beneficial for electron transfer between the electrolyte and electrode. Fig. 2e shows that the N 1s spectra of the catalyst can be deconvoluted into four peaks. The peaks centered at 394.8, 398.1, 399.2, and 401.5 eV can be ascribed to Mo/Ni–N_x, pyridinic N, pyrrolic N, and graphitic N, respectively. Notably, the peak percentage of pyridinic N in Ni-Mo_2C/CF is observably higher than that in Mo_2C. The four XPS peaks of C 1s (Fig. S5b) at 283.8, 284.8, 285.6, and 287.8 eV are indexed to C—Mo, C═C/C—C, C—N, and C═O [41]. The pyridinic N and C—N are mainly resulted from the nitrogen-doped carbon films. Particularly, the pyridinic N not only can improve electrical conductivity and surface wettability of the whole catalysts [42], but also modify the band density of carbon through accepting electrons from adjacent C atoms [43], thus facilitating the enhanced activity of the carbon films toward HER. As illustrated in Fig. 2d for the XPS spectrum of Ni in FeNi-Mo_2C/CF, as expected, the characteristic peaks of Ni^0 and Ni^{x+} are determined. Additionally, it can be found that the intensity of peaks of Ni^0 $2p_{3/2}$ in FeNi-Mo_2C/CF is weaker than that of Ni-Mo_2C/CF, resulting from that the chemical environment of Ni atoms has changed after being substituted by Fe atoms. Fig. 2f shows that there are three pairs of peaks in the high-resolution XPS of Fe in FeNi-Mo_2C/CF. The peaks at 707.7/720.4 eV are assigned to metallic iron (Fe^0). The peaks located at 710.9/724.2 eV can be attributed to Fe^{y+} (y greater than 2), which was ascribed to Fe—N or Fe—O bonds. The broad peak at around 713.0 eV can be attributed to an Auger peak of Auger Ni LMM [1]. And the other pair of peaks at 715.2/731.7 are associated to satellite peaks of Fe species. The high-resolution XPS of Fe (Fig. S5c) and that of Co (Fig. S5d) show the existence of Fe^0 in Fe-Mo_2C/CF and Co^0 in Co-Mo_2C/CF, respectively. The XPS peaks of Fe in Fe-/FeNi- Mo_2C/CF are also positively shifted as compared to the results reported by some researchers [1,28].

The microstructures of Mo_2C/CF (Fig. 3a–e, Fig. S6a–b), FeNi-Mo_2C/CF (Fig. 3f–j, Fig. S7a, b, Fig. S9a–f), and Ni-Mo_2C/CF (Fig. S10a–h) were further investigated by applying scanning electron microscopy (SEM) and transmission electron microscopy (TEM). The SEM images in Fig. 3a and f show that both Mo_2C/CF and FeNi-Mo_2C/CF possess a 3D porous flowerlike structure. The TEM images in Fig. 3b and g not only further indicate the porous flowerlike catalysts with about a diameter of 2 μm, but also reveal their hollow structure. The magnified SEM images in Fig. 3c and h suggest that the hollow microflower with mesopore and macropore channels is fabricated by numerous radiating outward nanosheets (petals) with an average thickness of 10 nm (Fig. S7a,b), and most of the edges of the nanosheets bend inward slightly resulting in a wrinkled and rough surface which can enhance the wettability of the catalysts. Other than the mesopore and macropore channels of the microflower, the sections circled by red circles in Fig. 3d and i show that there are also abundant micropores and mesopores on the petals, which correspond with the pore–size distribution analyzed by N_2 adsorption–desorption isotherms. The mesopore and macropore channels of the microflower can be interconnected by these micropores and

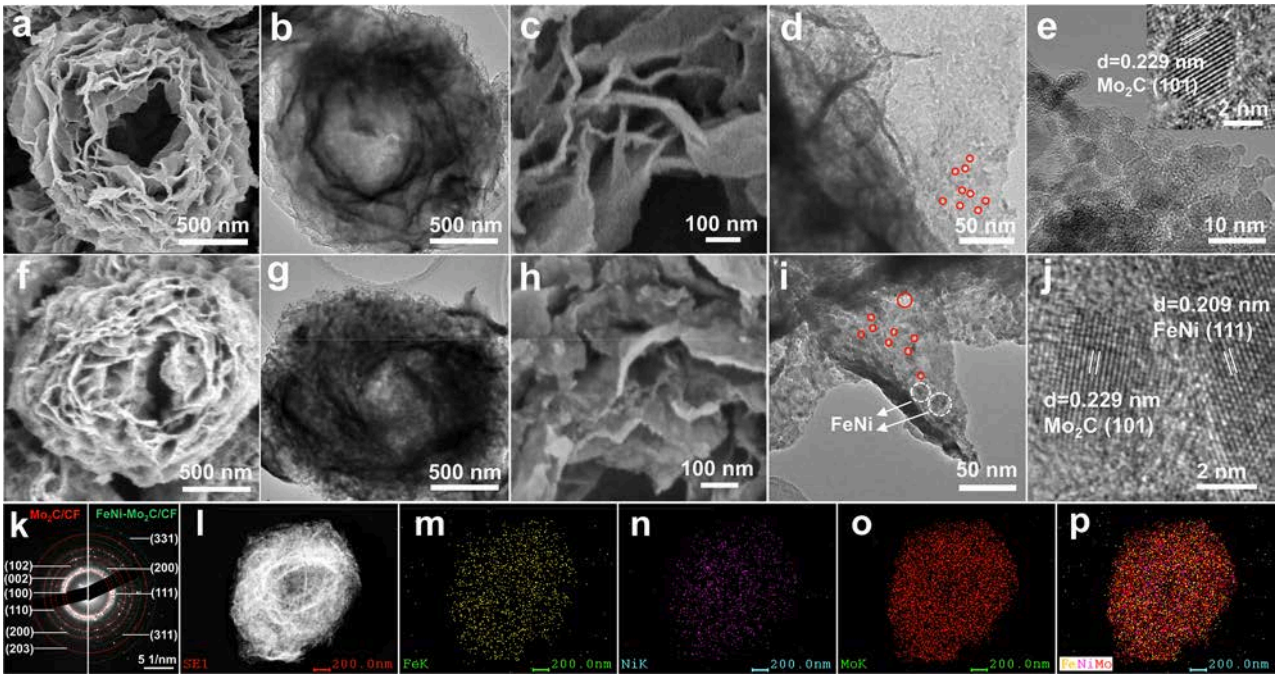

Fig. 3. Morphological and structural characterization of Mo_2C/CF and FeNi-Mo_2C/CF. (a,c) SEM images, (b,d) TEM images at different magnification and (e) High-resolution TEM image of Mo_2C/CF. (f,h) SEM images, (g,i) TEM images at different magnification and (j) High-resolution TEM image of FeNi-Mo_2C/CF. (k) SAED patterns of Mo_2C/CF and FeNi-Mo_2C/CF, respectively. (l–p) STEM image and the corresponding EDX mapping of FeNi-Mo_2C/CF.

mesopores. The interconnected micro- and mesoporous structures can facilitate electrolyte diffusion and the macroporous structure can act as an electrolyte reservoir, which can both effectively funnel the reactants and electrolytes into the active sites and facilitate the release of the bubbles. From the TEM images (Fig. 3d,e), it is clearly observed that the ultrathin petals of Mo_2C/CF microflower are actually constituted by Mo_2C nanoparticles (NPs) with a diameter of 5–7 nm densely and evenly embedded in the 2D carbon films (CF). In addition, lattice fringes with interplanar spacing of 0.229 nm can be observed from the high-resolution transmission electron microscopy (HRTEM) image (inset in Fig. 3e), which correspond to the (1 0 1) facet of β-Mo_2C. Meanwhile, energy dispersive X-ray (EDX) mapping was performed to further elucidate the elemental distributions over the Mo_2C/CF (Fig. S6a), revealing a homogeneous distribution of Mo, N, and C in the hybrid. The thermal gravimetric analysis of Mo_2C/CF (Fig. S8) shows that the weight percent of Mo_2C NPs is estimated to 84.9% (Eq. S1), indicating that the nitrogen-doped carbon films account for 15.1%. As shown in Fig. S6b, a 5–7 nm diameter of Mo_2C NPs are laterally cohered by the N-doped carbon as the binder to composed the average 10 nm thickness of petals of the Mo_2C/CF. Hence, Mo_2C NPs are evenly dispersed in the N-doped carbon film to endow the Mo_2C/CF with a robust and unique framework, which can suppress the aggregation/corrosion of Mo_2C and adequately expose the active sites during electrocatalytic process. As can be seen from the SEM image (Fig. 3h) and TEM image (Fig. 3i) of FeNi-Mo_2C/CF, a large number of nanoparticles with a 10–20 nm diameter, which can be demonstrated as FeNi alloy nanoparticles according to the following analysis of energy dispersive X-ray spectrum (EDS), elemental mapping, and HRTEM measurements, are evenly distributed on Mo_2C/CF to fabricate the unique architecture of FeNi-Mo_2C/CF. As shown in the HRTEM image (Fig. 3j), nanoparticles with a lattice spacing of 0.229 nm and with a lattice spacing of 0.209 can be detected in FeNi-Mo_2C/CF, which are assigned to the (1 0 1) facet of β-Mo_2C and the (1 1 1) facet of FeNi alloy, respectively. Fig. 3b exhibits the selected area electron diffraction (SAED) pattern and the Debye–Scherrer rings can be indexed by FeNi alloy and β-Mo_2C, meanwhile, the halo feature at the center can be ascribed to the amorphous carbon which fabricated the carbon films. Fig. 3l displays a scanning transmission electron microscopy (STEM) image of FeNi-Mo_2C/CF and the corresponding STEM-EDS elemental mapping (Fig. 3m–p) clearly demonstrate the uniform distribution of Fe, Ni, and Mo elements, which suggests a homogeneous dispersion of FeNi alloy NPs and Mo_2C NPs in the entire CF. The energy dispersive X-ray spectrum (Fig. S9a) exhibits Fe, Ni, Mo, C, N, and O signals in FeNi-Mo_2C/CF. Moreover, the high-angle annular dark-field scanning transmission electron microscopy (HAADF-STEM) image with nanometer resolution (Fig. S9b) and the corresponding EDS elemental mappings (Fig. S9c-f) further reveal that FeNi alloy NPs are immobilized on Mo_2C/CF. The TEM image in Fig. S10a shows that the Ni-Mo_2C/CF features with similar morphology to that of FeNi-Mo_2C/CF. The circled section with the red rectangle in the HRTEM image (Fig. S10b) exhibits some interconnected NPs in the Ni-Mo_2C/CF and the corresponding inverse fast Fourier transform (IFFT) image (Fig. S10c) shows two distinct lattice spacings and a noteworthy interface between them. The NP with a lattice distance of 0.206 nm can be indexed to (1 1 1) plane of cubic Ni and the other with 0.229 nm lattice distances is assigned to (1 0 1) plane of β-Mo_2C. The heterostructure composed of Ni strongly coupled with Mo_2C offers more opportunity for efficient electron transfer and synergistic effect. The SAED pattern in Fig. S10d indicates that Ni, Mo_2C, and amorphous CF are coexistence in Ni-Mo_2C/CF. The EDS (Fig. S10e) exhibits Ni, Mo, C, N, and O signals in Ni-Mo_2C/CF and the EDS mappings (Fig. S10g–h) obviously suggest a homogeneous dispersion of Ni NPs on the Mo_2C/CF and the successful introduction of N which can effectively adjust the electronic structure of the carbon matrix. This distinct structure and composition provide the samples with plenty of active sites in a three-dimensional direction and an improved conductivity. Meanwhile, C—N bonds from the nitrogen-doped CF and Ni—N bonds from the surface of Ni NPs are co-existence in Ni-Mo_2C/CF, thereby, benefitting from the covalently bonding interaction of Ni—N—C, Ni NPs can tightly attached to the CF. Moreover, there are plentiful electron transfer resulting from the heterointerfaces between Ni and Mo_2C which is demonstrated by the XRD and XPS characterization of Ni-Mo_2C/CF. Thus, Ni NPs, Mo_2C NPs, and the CF assemble the robust heterostructure of Ni-Mo_2C/CF and construct numerous heterointerfaces which will contribute to their strong synergistic effect during HER.

In addition, a measurement of contact angles (CAs) was performed to analyze the wettability, and the value was calculated after the elapse of 30 s when 1 μL of KOH solution was dropped on the surface of working electrode. The CAs are 76.5° and 49.6° for glass carbon electrode and pristine Mo_2C/CF, respectively. In contrast, the CAs of Ni-Mo_2C/CF and FeNi-Mo_2C/CF decrease to 34.3° and 29.1° (Fig. S11), respectively, revealing a much more hydrophilic surface. The lower CAs of Ni-Mo_2C/CF and FeNi-Mo_2C/CF could be ascribed to their trimodal-porous structures, rough surface and increased content of pyridinic N. On the basis of the interface theory of solid–liquid–gas, structures with roughness at both micro- and nanoscale can boost the release of bubbles and promote the wettability toward the electrolyte, and the porous structures provide abundant open channels for rapid electrolyte diffusion, bubbles release, and electron transport, which can expedite the mass transfer and the reaction kinetics and contribute to reaction stability [44].

Based on the above characterizations and analyses, the unique trimodal-porous structures, microsize dimension, and compositions of Ni-Mo_2C/CF and FeNi-Mo_2C/CF provide the samples with plenty of active sites, robust heterostructures, channels for rapid mass transport and electron/ion transfer, high-efficiency synergistic effect for highly intrinsic activity, and the improved conductivity for the fast exchange of charge. Accordingly, Ni-Mo_2C/CF and FeNi-Mo_2C/CF are expected to exhibit promising electrocatalytic activity.

2.2. Electrocatalytic performances of Ni-Mo_2C/CF toward HER

The HER performances of Ni-Mo_2C/CF were investigated in a three-electrode cell under alkaline condition of N_2-saturated 1.0 M KOH solution. To compare and contrast, the electrochemical performances of 20% Pt/C for HER were also assessed. Fig. 4a shows the linear scan voltammetry (LSV) curves of the prepared samples. The commercial 20% Pt/C shows a better HER activity with a near zero onset potential and 39 mV at current density of 1 and 10 mA cm^{-2}, respectively. However, as shown in Fig. S12, the required overpotential of 5.8% Ni-Mo_2C/CF is lower than that of commercial Pt/C to attain a current density larger than 93 mA cm^{-2}, revealing that 5.8% Ni-Mo_2C/CF works better than the commercial Pt/C at high current density in 1.0 M KOH. The Ni-Mo_2C/CF exhibits a much better HER activity compared to Mo_2C/CF, indicating the existence of a synergistic effect between Ni and Mo_2C. Furthermore, the content of Ni makes a difference to the catalytic activity of Ni-Mo_2C/CF. To drive 10/50 mA cm^{-2}, the Mo_2C/CF, 4.3% Ni-Mo_2C/CF, 5.8% Ni-Mo_2C/CF and 6.9% Ni-Mo_2C/CF require overpotentials of 138/194, 107/159, 81/120, and 107/170 mV, respectively. To further evaluate the catalytic performances of Ni-Mo_2C/CF, the HER kinetics were investigated with Tafel slopes. Fig. 4c exhibits the corresponding Tafel plots. The Tafel slope of 20% Pt/C is 40.6 mV dec^{-1}, and 0%, 4.3%, 5.8%, and 6.9% Ni-Mo_2C/CF perform Tafel slopes of 57.6, 50.7, 43.5, and 60.8 mV dec^{-1}, respectively. In general, the lower Tafel slope suggests faster reaction kinetic, and 5.8% Ni-Mo_2C/CF performs faster catalytic kinetic during HER than other x% Ni-Mo_2C/CF. As well known, Tafel slopes of 120, 40, and 30 mV dec^{-1} correspond to the Volmer, Heyrovsky, and Tafel process, respectively, suggesting that the reaction proceeds through the Volmer–Heyrovsky mechanism [45]. To better investigate the improved performance for Ni-Mo_2C/CF, electrochemical impedance spectroscopy (EIS) measurements were performed. The representative Nyquist plots of x% Ni-Mo_2C/CF and Mo_2C/CF are shown in Fig. 4c and the inset is an equivalent circuit model for

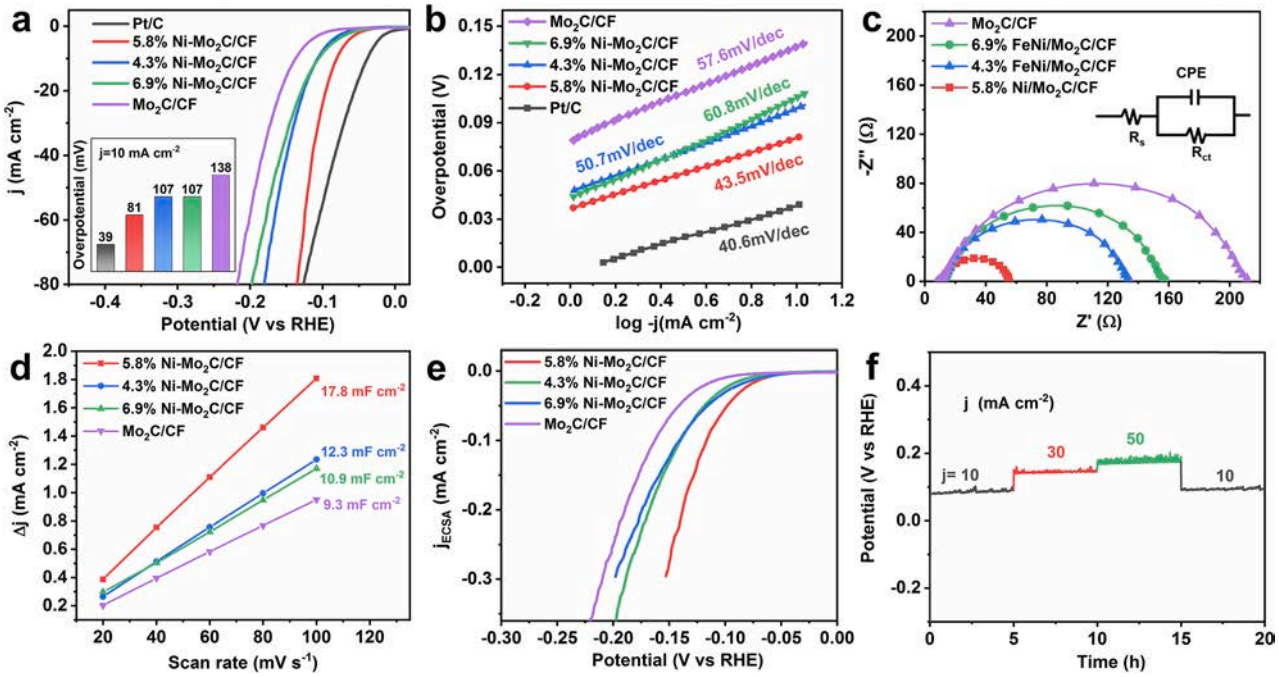

Fig. 4. Alkaline HER investigations of Ni-Mo_2C/CF heterostructure. (a) LSV curves of *x*% Ni-Mo_2C/CF, Mo_2C/CF, and commercial Pt/C; Inset: Overpotential to achieve 10 mA cm^{-2}. (b) The corresponding Tafel plots. (c–e) EIS spectra, C_{dl} curves, and LSV curves normalized by ECSA of *x*% Ni-Mo_2C/CF and Mo_2C/CF toward HER. Inset of (c): The electrical equivalent circuit used for fitting EIS. (f) Chronopotentiometric curves toward HER of the 5.8% Ni-Mo_2C/CF heterostructure at various current densities.

electrochemical impedance tests. The R_{ct} which can be calculated from the radius of semicircle in high frequency region represents the charge transfer resistance between catalyst surface and electrolyte. It is can be found that 5.8% Ni-Mo_2C/CF presents the shortest semicircle among all investigated samples, indicating the fastest electron-transfer rate and the fastest kinetics. The electrochemical active surface area (ECSA) is a reflection of the surface area of a catalyst accessible to the catalytic reactions, which is directly proportional to the double-layer capacitance (C_{dl}). The values of C_{dl} were determined by Cyclic voltammetry (CV) at various scan rates in the non-faradaic potential range (Fig. S13). Particularly, as depicted in Fig. 4d, the C_{dl} of 5.8% Ni-Mo_2C/CF is 17.8 mF cm^{-2}, higher than 10.9 mF cm^{-2} of 4.3% Ni-Mo_2C/CF and 9.3 mF cm^{-2} of Mo_2C/CF, indicating that the increase of Ni concentration can generate more interfaces between Ni and Mo_2C NPs and improve their synergistic effect. However, the C_{dl} of 6.9% Ni-Mo_2C/CF is 12.3 mF cm^{-2}, smaller than that of 5.8% Ni-Mo_2C/CF, revealing that the superfluous Ni NPs of 6.9% Ni-Mo_2C/CF may cover the active sites which originate from Mo_2C NPs or the interfaces between Ni and Mo_2C NPs. From the aforementioned results, it is apparently concluded that 5.8% Ni-Mo_2C/CF shows the best HER activity. Nevertheless, the intrinsic catalytic activity of the catalyst can be more fundamental for increasing the water splitting performance. In order to further evaluate intrinsic electrocatalytic activities of Ni-Mo_2C/CF for HER, the specific activity was obtained by normalizing the current densities with the ECSA. As revealed in Fig. 4e, 5.8% Ni-Mo_2C/CF still shows superior HER activities to Mo_2C/CF, 4.3% Ni-Mo_2C/CF, and 6.9% Ni-Mo_2C/CF despite normalizing the current densities with the ECSA, indicating the optimal synergy effect among Mo_2C NPs, Ni NPs, and the N-doped CF in 5.8% Ni-Mo_2C/CF. Electrochemical stability is another critical factor for the practical application of electrocatalysts. Here, we probed the long-term stability of 5.8% Ni-Mo_2C/CF by testing at four constant current densities of 10, 30, 50, and 10 mA cm^{-2} for 20 h, and we found that the potentials exhibited negligible changes, implying the robust HER stability of the 5.8% Ni-Mo_2C/CF in addition to superior activity. In addition, the 5.8% Ni-Mo_2C/CF also demonstrates prominent HER performance when compared comprehensively with other Ni- and Mo-based electrocatalysts (Table S3).

2.3. *Electrocatalytic performances of FeNi-Mo_2C/CF toward OER*

The OER activities of as-prepared Fe-, FeCo-, and FeNi-Mo_2C/CF were evaluated in an O_2-saturated 1.0 M KOH solution. M(M = Co, Ni)-Mo_2C/CF and commercial nickel foam were tested in a purified (Fe free) KOH solution. As a reference, a commercial RuO_2 catalyst was also measured. The OER performance was assessed when reproducible LSV curves were obtained. As shown in Fig. S14a, Ni-Mo_2C/CF affords 10 mA cm^{-2} at an overpotencial of 345 mV, much lower than those of the commercial nickel foam (485 mV) and Mo_2C/CF (490 mV). In addition, the OER activity of Ni-Mo_2C/CF is comparable and even better than those of many reported representative Ni/Mo_2C-based electrocatalysts (Table S4), suggesting that the strategy to construct Ni-Mo_2C/CF is favorable for improving the OER activity of the Ni/Mo_2C-based material. Meanwhile, the same strategy is adopt to construct FeNi-Mo_2C/CF, Fe-Mo_2C/CF, Co-Mo_2C/CF, and FeCo-Mo_2C/CF, revealing its universality. As illustrated in Fig. 5a, FeNi-Mo_2C/CF exhibits superior OER activities than FeCo-, Ni-, Co-, and Fe-Mo_2C/CF. It is worth noting that FeNi-Mo_2C/CF and FeCo-Mo_2C/CF show remarkably enhanced OER performances compared to Ni-Mo_2C/CF and Co-Mo_2C/CF respectively, suggesting that Fe substitution plays a key role for the outstanding performance. Among the *x* FeNi-Mo_2C/CF samples, with the increase of the mole ratio of Fe to Ni, the OER catalytic performances present significant improvement initially with subsequent degradation, and 0.7 FeNi-Mo_2C/CF shows the optimum performance. The inset in Fig. 5a is an enlargement image of the LSV curves, shows that there is an anodic peak before the OER onset. Since the anodic transitions from metallic Fe to Fe^{2+}/Fe^{3+} occur at around 0.4 V (RHE), the Fe does not have any redox features in this potential range and remains nominally Fe^{3+}. This peak is attributed to the oxidation of Ni^{2+}/Ni^{3+}, which is corresponding to the oxidation of $Ni(OH)_2$ to NiOOH [46]. It can be further proved by the presence of peaks of Fe^{3+} and Ni^{3+} in FeNi-Mo_2C/CF (Fig. S15a,b) after the steady voltammogram curves were obtained for OER. It has been reported that the electronic structure of NiOOH varies with Fe

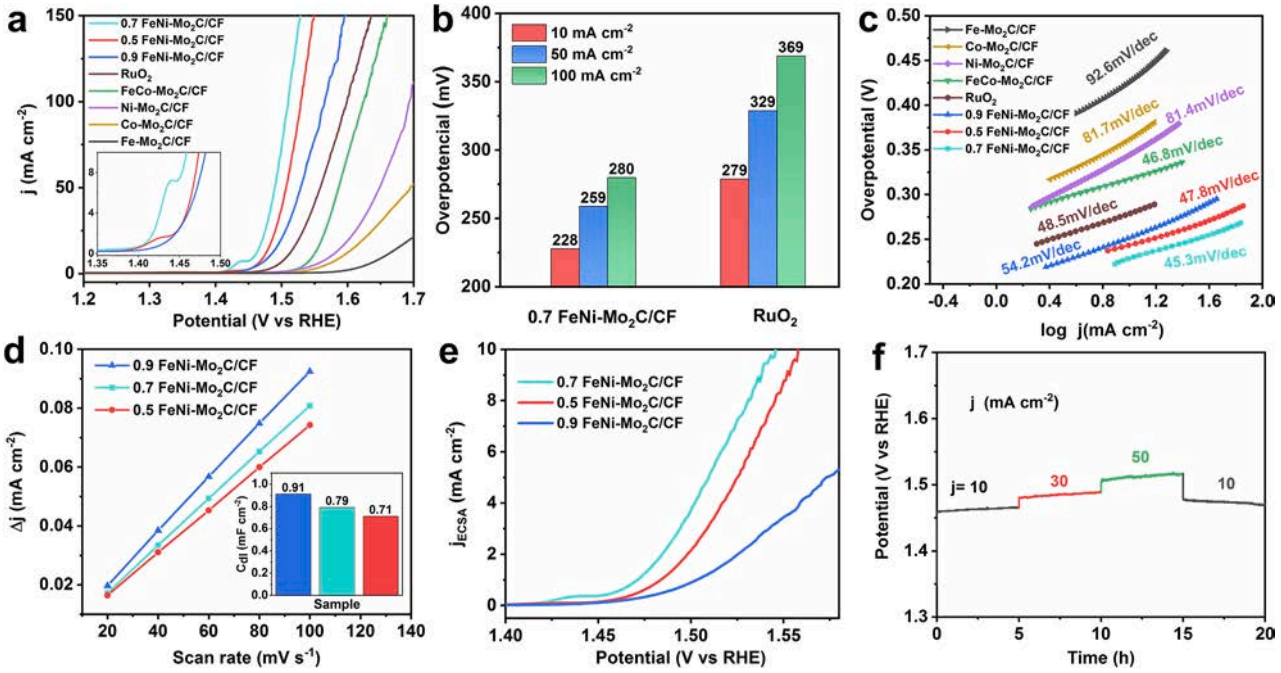

Fig. 5. Electrocatalytic OER of FeNi-Mo_2C/CF heterostructure. (a) LSV curves of different catalysts. Inset: Expanded view of the low-overpotential region of *x* FeNi-Mo_2C/CF toward OER. (b) Comparisons of overpotential at 10, 50, 100 mA cm^{-2} for 0.7 FeNi-Mo_2C/CF with commercial RuO_2. (c) The corresponding Tafel plots. (d–e) C_{dl} curves and LSV curves normalized by ECSA of × FeNi-Mo_2C/CF. Inset of (d): The calculated of *C*dl slops. (f) Chronopotentiometric curves toward OER of 0.7 FeNi-Mo_2C/CF heterostructure at various current densities.

content and thus affects the OER activity [33]. Here, we can observe that the Ni^{2+}/Ni^{3+} waves shift to higher potentials with the increase of Fe content, indicating a strong electronic interaction between Ni and Fe that modifies the electronic structure of the activated catalyst. The different shifts (1.36 to 1.44 V vs. RHE) of oxidation peak of Ni^{2+}/Ni^{3+} (Fig. 5a and Fig. S14b) demonstrate the change in the electronic structure of *x* FeNi-Mo_2C/CF samples. Consequently, it is believed that the 0.7 FeNi-Mo_2C/CF displaying the optimum catalytic activity is due to the most favorable electronic configuration among the *x* FeNi-Mo_2C/CF samples. Notably, as shown in Fig. 5b, the 0.7 FeNi-Mo_2C/CF affords 228, 259, and 280 mV to deliver 10, 50, and 100 mA cm^{-2}, respectively, superior to the commercial RuO_2 (279, 329, and 369 mV). As presented in Fig. 5c, 0.7 FeNi-Mo_2C/CF shows the smallest Tafel slope (45.3 mV dec^{-1}), exhibiting the fastest dynamics of OER among the samples. Impressively, the Tafel slopes of FeNi- and FeCo-Mo_2C/CF are remarkably lower than that of Fe-, Ni-, and Co-Mo_2C/CF, showing that the interaction of different metals in alloy significantly affects the kinetics of water oxidation. Generally, it can be inferred by the Tafel slope that which of the four electron-/proton-transfer steps (Eq. S2) is the rate limiting in the OER. For a chemically reversible multistep reaction with a single rate-determining step (in the classical Butler-Volmer formalism), the Tafel slope is given by (59 mV dec^{-1})/(n′+α), where n′ is the number of single-electrontransfer steps prior to the rate-determining step and α is the symmetry/transfer coefficient (typically taken as 0.5) [32]. The FeNi-/FeCo-Mo_2C/CF have Tafel slopes of 45–54 mV dec^{-1}, implying that the second electron transfer is the rate determining. While Tafel slopes of 81–92 mV dec^{-1} are associated with a rate-limiting chemical step following the first electron transfer for Fe-/Ni-/Co-Mo_2C/CF. Furthermore, as shown in Fig. 5d, the C_{dl} data which are determined by cyclic voltammetry (CV) at various scan rates in the non-faradaic potential range (Fig. S16) indicates that 0.7 FeNi-Mo_2C/CF owns fewer active sites than 0.9 FeNi-Mo_2C/CF. Nevertheless, the LSV curves in Fig. 5e show that 0.7 FeNi-Mo_2C/CF exhibits the best OER performance despite normalizing the current densities with the ECSA, suggesting that 0.7 FeNi-Mo_2C/CF has the highest intrinsic catalytic activity. Furthermore, after a stability test for 20 h, the potentials of 0.7 FeNi-Mo_2C/CF at various current densities of 10, 30, and 50 mA cm^{-2} only display increases of 7, 8, and 12 mV, respectively, further demonstrating the outstanding OER stability of 0.7 FeNi-Mo_2C/CF. Also, the OER activities of FeNi-Mo_2C/CF are comparable or superior to most other FeNi-based electrocatalysts reported in alkaline solution (Table S4).

Remarkably, FeNi-Mo_2C/CF is also superior to the Fe-//Ni-Mo_2C/CF (Fig. S14a, Table S4), indicating that FeNi alloy NPs on the surface of Mo_2C/CF play an important role for the enhanced OER activity in 1.0 M KOH. To gain further insight into its remarkable OER activity, compositional and structural evolutions of 0.7 FeNi-Mo_2C/CF after long-term OER stability test were investigated with XRD, TEM, HAADF-STEM, EDS-mapping, XPS, and SEM. The sample after OER stability test was marked as FeNi-Mo_2C/CF-a. The XRD pattern of FeNi-Mo_2C/CF-a (Fig. S17a) and HRTEM image as well as the corresponding FFT and IFFT (Fig. S17b) exhibit the partial oxidation of Mo_2C to MoO_2, which is consistent with the results in the previous report [24]. On the other hand, the diffraction peaks of FeNi alloy decrease, which is due to the oxidation of its surface. The HRTEM image of FeNi-a NPs in FeNi-Mo_2C/CF-a (Fig. 6a) shows a core–shell structure: the core part remains conductive FeNi alloy phase while the shell part with a thickness of approximate 2 nm is amorphous. A few reports have revealed that the surface species will finally transform into oxyhydroxides during OER process in alkaline electrolyte [1]. Thus, the amorphous shell of FeNi-a NPs can be ascribed to FeNi-oxyhydroxides which are in-situ generation on the surface of FeNi alloy NPs. The STEM-EDS-mappings of FeNi-Mo_2C/CF-a (Fig. S17c) reveal the existence of Fe, Ni and O elements on the surface of FeNi-a NPs, suggesting the Fe and Ni atoms on surface were transformed into FeNi-oxyhydroxide, which is in good agreement with the results of the following XPS of depth profiles. Generally, oxyhydroxides generated during water oxidation is considered as veritable active species for OER [4]. Herein, the small lateral size and ultrathin thickness of these FeNi-oxyhydroxides on the surface of the conductive FeNi NPs enable the sufficient exposure of active sites and favorable reduction of the transport resistance of electrons from the surface catalyst to the electrode, and this ability are further enhanced by the

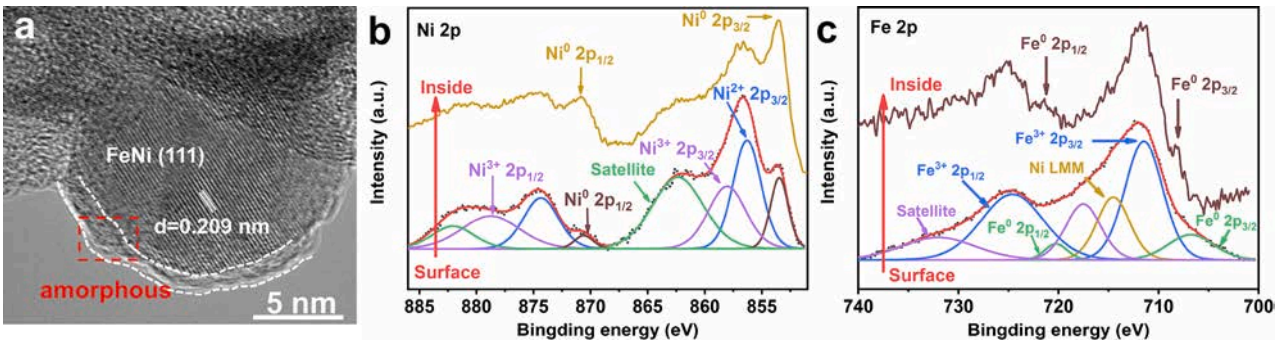

Fig. 6. Morphological and structural characterization of FeNi-Mo_2C/CF after OER stability test. (a) TEM image of FeNi-a nanoparticles. (b) XPS depth profile of Ni 2p and (c) Fe 2p for FeNi-Mo_2C/CF after OER testing.

conductive porous Mo_2C/CF as the substrate. The XPS of depth profiles for Ni 2p and further confirms the existence of FeNi-oxyhydroxides, as shown in Fig. 6a and b. Notably, the peaks of Ni^{3+} were determined through fitting the high-resolution XPS of Ni in FeNi-Mo_2C/CF-a (Fig. 6b), revealing that Ni^0 and Ni^{x+} on the surface of FeNi NPs were oxidized during the OER process. On the other hand, the high-resolution XPS of Fe in FeNi-Mo_2C/CF-a (Fig. 6c) shows a pair of peaks at 711.6/725.0 eV, which are higher than 710.9/724.2 eV of Fe^{y+} in FeNi-Mo_2C/CF. Accordingly, it can be assigned to Fe^{3+}, confirming the oxidation of Fe^0 and Fe^{y+} at OER potentials. The presence of Fe^{3+} and Ni^{3+} support the production of the thin FeNi-oxyhydroxides layers on the surface of FeNi alloy NPs. The signals of metallic Ni and metallic Fe are enhanced after etched by argon ion beam, with the reduction of oxidation state signals of Ni and Fe. Therefore, the FeNi-oxyhydroxide is critical active specie for water oxidation.

Notably, SEM image (Fig. S19) indicates that porous structure can be well maintained after long-term OER test. The maintained porous structures enable the adequate exposure of active sites in a three-dimensional direction, promote the electrolyte diffusion in catalysts under capillary imbibition of connected porous structure, and boost the

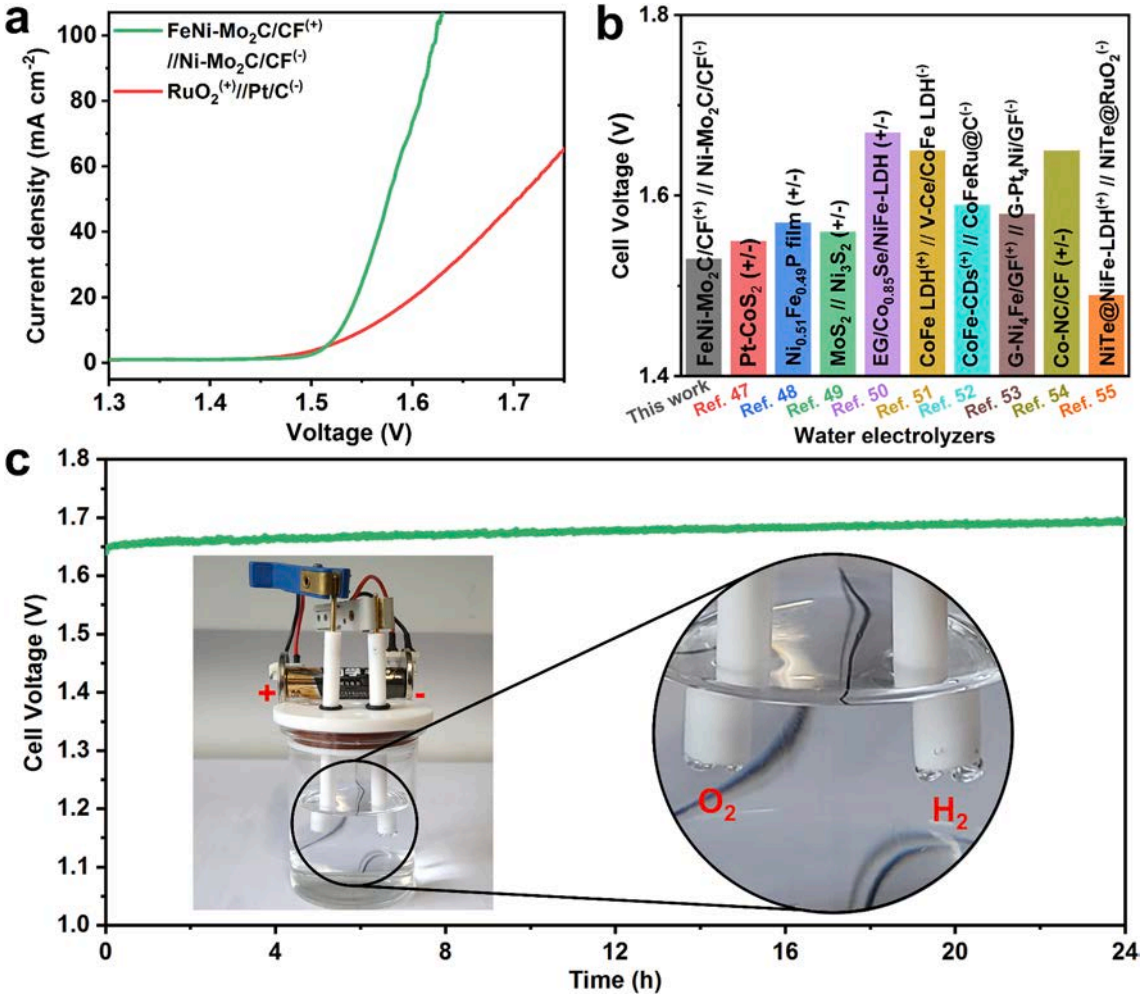

Fig. 7. Overall water splitting. (a) LSV curves of FeNi-Mo_2C/$CF^{(+)}$//Ni-Mo_2C/$CF^{(-)}$ electrolyzer and $RuO_2{}^{(+)}$//$Pt^{(-)}$ electrolyzer in 1.0 M KOH. (b) Comparison of the cell voltages to achieve 10 mA cm^{-2} for our designed electrolyzer with currently available robust electrolyzers. (c) Durability tests of this electrolyzer at 50 mA cm^{-2}.

release of bubbles during OER. Besides the compositions of FeNi-Mo_2C/CF-a, the unique trimodal-porous structure also plays a key role in the excellent electrochemical performance of OER. As shown in Fig. S19a, FeNi/CB (FeNi alloy mixed with carbon black, and the details for the synthesis procedures see Supporting Information) requires 47 mV and 60 mV larger than FeNi-Mo_2C/CF to attain 10 and 20 mA cm^{-2}, respectively. The Tafel slope (Fig. S19b) of FeNi-Mo_2C/CF (45.3 mV dec^{-1}) is lower than that of FeNi/CB (57.6 mV dec^{-1}), indicating FeNi alloy NPs with Mo_2C/CF can exhibit higher OER performance and faster kinetics compared with the alloy powder with carbon black. Furthermore, the section above 50 mA cm^{-1} of the LSV curve of FeNi/CB reveals a non-smooth curve, due to the restriction of electrolyte diffusion by the adhesive bubbles generated on the surface of the electrode. Besides, it can be found that the anodic peak of FeNi/CB (inset of Fig. S19a) is weaker than that of FeNi-Mo_2C/CF, indicating less hydroxide/oxyhydroxide on the surface than that of FeNi-Mo_2C/CF. The contact angles (Fig. S19c) of FeNi/CB and FeNi-Mo_2C/CF after OER are 51.7° and 25.3°, respectively, indicating that FeNi-Mo_2C/CF is more hydrophilic than FeNi/CB. From another perspective, these results prove that FeNi-Mo_2C/CF with trimodal-porous and microsize structure can facilitate the exposure of active sites and the mass transport.

2.4. Evaluation of the electrocatalytic overall water splitting performance

Inspired by the favorable activities as well as stabilities of Ni-Mo_2C/CF for HER and FeNi-Mo_2C/CF for OER, we paired Ni-Mo_2C/CF as cathode and FeNi-Mo_2C/CF as anode to assemble an alkaline electrolyzer for overall water splitting. A water electrolyzer with $RuO_2^{(+)}$//Pt/$C^{(-)}$ was fabricated for comparison. Their steady-state potential polarization curves are presented in Fig. 7a, showing that the FeNi-Mo_2C/$CF^{(+)}$//Ni-Mo_2C/$CF^{(-)}$ electrolyzer requires only a cell voltage of 1.53 V to achieve a water-splitting current density of 10 mA cm^{-2}, which is superior to the coupled benchmarking RuO_2–Pt/C catalysts (1.556 V). This result is also comparable or superior to most of previously reported remarkable full-cells for overall water splitting [47–55], as shown in Fig .7b. Additionally, the cell is successfully driven by a battery of 1.5 V, as shown in Video-S1 and the inset of Fig. 7c. As for the electrochemical durability, the test is conducted by chronopotentiometry with a high current density of 50 mA cm^{-2}, and it sustains an overall-water-splitting performance with negligible decay for over 24 h.

3. Conclusions

In summary, we report a novel method to fabricate a highly active and robust heterojunction catalyst composed of 3D N-doped carbon films integrated with ultrasmall Ni (FeNi alloy) and Mo_2C nanoparticles (Ni-(FeNi-)Mo_2C/CF) for water splitting. The synthetic catalysts with trimodal-porous structure and microsize dimension facilitate the exposure of active sites and mass transport. The content of Ni in Ni-Mo_2C/CF and the mole ratio of Fe to Ni in FeNi-Mo_2C/CF are optimized to achieve a superior HER and OER performance, respectively. The optimized Ni-Mo_2C/CF achieves a low overpotential of 81 mV to reach 10 mA cm^{-2} with a small Tafel slope of 43.5 mV dec^{-1} in 1.0 M KOH, displays a much better HER activity compared to Mo_2C/CF, and exhibits remarkable stability. Moreover, it performs better than the commercial Pt/C at high current density. On the other hand, the optimized FeNi-Mo_2C/CF requires an ultralow overpotential of 228 mV at 10 mA cm^{-2} with a low Tafel slope of 45.3 mV dec^{-1} toward OER, outperforming the benchmark RuO_2 (279 mV, 48.5 mV dec^{-1}). In particular, we construct a FeNi-Mo_2C/$CF^{(+)}$//Ni-Mo_2C/$CF^{(-)}$ alkaline water electrolyzer, all being inexpensive materials, which demonstrates a low cell voltage of 1.53 V at 10 mA cm^{-2}, superior to the coupled benchmarking RuO_2–Pt catalysts (1.556 V) and most of previously reported remarkable full-cells for overall water splitting. Furthermore, our designed electrolyzer shows impressive stability over 24 h at 50 mA cm^{-2}. This work provides a facile and effective method to construct high-performance and non-precious metal electrocatalysts for commercial water splitting.

4. Experimental section

The details for the synthesis procedures, structural characterization and electrochemical measurements see Supporting Information.

Declaration of Competing Interest

The authors declare that they have no known competing financial interests or personal relationships that could have appeared to influence the work reported in this paper.

Acknowledgements

This work was financially supported by the National Natural Science Foundation of China (Grant No. 22078233) and National Key R&D Program of China (No. 2017YFB0602702-02).

Appendix A. Supplementary data

Supplementary data to this article can be found online at https://doi.org/10.1016/j.cej.2021.131712.

References

[1] C. Liang, P. Zou, A. Nairan, Y. Zhang, J. Liu, K. Liu, S. Hu, F. Kang, H.J. Fan, C. Yang, Exceptional performance of hierarchical Ni-Fe oxyhydroxide@NiFe alloy nanowire array electrocatalysts for large current density water splitting, Energy Environ. Sci. 13 (1) (2020) 86–95, https://doi.org/10.1039/c9ee02388g.
[2] M. Khalid, X. Zarate, M. Saavedra-Torres, E. Schott, A. Maria Borges Honorato, M. Rafe Hatshan, H. Varela, Electro-reduced graphene oxide nanosheets coupled with RuAu bimetallic nanoparticles for efficient hydrogen evolution electrocatalysis, Chem. Eng. J. 421 (2021) 129987, https://doi.org/10.1016/j.cej.2021.129987.
[3] P. Zhang, L. Li, D. Nordlund, H. Chen, L. Fan, B. Zhang, X. Sheng, Q. Daniel, L. Sun, Dendritic core-shell nickel-iron-copper metal/metal oxide electrode for efficient electrocatalytic water oxidation, Nat. Commun. 9 (1) (2018), https://doi.org/10.1038/s41467-017-02429-9.
[4] Y.J. Zhou, Y.H. Li, L.X. Zhang, L.L. Zhang, L. Li, J.J. Tian, M. Wang, J.Y. Xu, B. Dai, Y.S. Li, Fe-leaching induced surface reconstruction of Ni-Fe alloy on N-doped carbon to boost oxygen evolution reaction, Chem. Eng. J. 394 (2020) 10, https://doi.org/10.1016/j.cej.2020.124977.
[5] P. Chen, T. Zhou, M. Chen, Y. Tong, N. Zhang, X. Peng, W. Chu, X. Wu, C. Wu, Y. Xie, Enhanced catalytic activity in nitrogen-anion modified metallic cobalt disulfide porous nanowire arrays for hydrogen evolution, ACS Catal. 7 (11) (2017) 7405–7411, https://doi.org/10.1021/acscatal.7b02218.
[6] J.Y. Zhang, H.M. Wang, Y.F. Tian, Y. Yan, Q. Xue, T. He, H.F. Liu, C.D. Wang, Y. Chen, B.Y. Xia, Anodic hydrazine oxidation assists energy-efficient hydrogen evolution over a bifunctional cobalt perselenide nanosheet electrode, Angew. Chem. Int. Edit. 57 (26) (2018) 7649–7653, https://doi.org/10.1002/anie.201803543.
[7] B. Zhang, X. Zheng, O. Voznyy, R. Comin, M. Bajdich, M. Garcia-Melchor, L. Han, J. Xu, M. Liu, L. Zheng, F.P.G. de Arquer, C.T. Dinh, F. Fan, M. Yuan, E. Yassitepe, N. Chen, T. Regier, P. Liu, Y. Li, P. De Luna, A. Janmohamed, H.L. Xin, H. Yang, A. Vojvodic, E.H. Sargent, Homogeneously dispersed multimetal oxygen-evolving catalysts, Science 352 (6283) (2016) 333–337, https://doi.org/10.1126/science.aaf1525.
[8] M. Kim, B. Lee, H. Ju, S.W. Lee, J. Kim, Reducing the barrier energy of self-reconstruction for anchored cobalt nanoparticles as highly active oxygen evolution electrocatalyst, Adv. Mater. 31 (32) (2019), https://doi.org/10.1002/adma.201901977.
[9] H. Yang, J. Liu, Z. Chen, R. Wang, B. Fei, H. Liu, Y. Guo, R. Wu, Unconventional bi-vacancies activating inert Prussian blue analogues nanocubes for efficient hydrogen evolution, Chem. Eng. J. (2020), 127671, https://doi.org/10.1016/j.cej.2020.127671.
[10] L.C. Seitz, C.F. Dickens, K. Nishio, Y. Hikita, J. Montoya, A. Doyle, C. Kirk, A. Vojvodic, H.Y. Hwang, J.K. Norskov, T.F. Jaramillo, A highly active and stable IrOx/$SrIrO_3$ catalyst for the oxygen evolution reaction, Science 353 (6303) (2016) 1011–1014, https://doi.org/10.1126/science.aaf5050.
[11] B. Geng, F. Yan, L. Liu, C. Zhu, B. Li, Y. Chen, Ni/MoC heteronanoparticles encapsulated within nitrogen-doped carbon nanotube arrays as highly efficient self-supported electrodes for overall water splitting, Chem. Eng. J. 406 (2021) 126815, https://doi.org/10.1016/j.cej.2020.126815.
[12] Y. Sun, F. Peng, L. Zhang, B. Jiang, H. Dou, N. Zhang, M. Xu, N. Yang, Hierarchical nitrogen-doped Mo_2C nanoparticle-in-microflower electrocatalyst: in situ synthesis and efficient hydrogen-evolving performance in alkaline and acidic media,

Chemcatchem 12 (23) (2020) 6040–6049, https://doi.org/10.1002/cctc.202000995.
[13] K. Peng, H. Wang, H. Gao, P. Wan, M. Ma, X. Li, Emerging hierarchical ternary 2D nanocomposites constructed from montmorillonite, graphene and MoS_2 for enhanced electrochemical hydrogen evolution, Chem. Eng. J. 393 (2020) 124704, https://doi.org/10.1016/j.cej.2020.124704.
[14] C. Wan, Y.N. Regmi, B.M. Leonard, Multiple phases of molybdenum carbide as electrocatalysts for the hydrogen evolution reaction, Angew. Chem. Int. Edit. 53 (25) (2014) 6407–6410, https://doi.org/10.1002/anie.201402998.
[15] H.L. Lin, Z.P. Shi, S.N. He, X. Yu, S.N. Wang, Q.S. Gao, Y. Tang, Heteronanowires of MoC-Mo_2C as efficient electrocatalysts for hydrogen evolution reaction, Chem. Sci. 7 (5) (2016) 3399–3405, https://doi.org/10.1039/c6sc00077k.
[16] L. Liao, S.N. Wang, J.J. Xiao, X.J. Bian, Y.H. Zhang, M.D. Scanlon, X.L. Hu, Y. Tang, B.H. Liu, H.H. Girault, A nanoporous molybdenum carbide nanowire as an electrocatalyst for hydrogen evolution reaction, Energy Environ. Sci. 7 (1) (2014) 387–392, https://doi.org/10.1039/c3ee42441c.
[17] W.W. Han, L.L. Chen, B. Ma, J. Wang, W.Y. Song, X.B. Fan, Y. Li, F.B. Zhang, W. C. Peng, Ultra-small Mo_2C nanodots encapsulated in nitrogen-doped porous carbon for pH-universal hydrogen evolution: insights into the synergistic enhancement of HER activity by nitrogen doping and structural defects, J. Mater. Chem. A 7 (9) (2019) 4734–4743, https://doi.org/10.1039/c8ta11098k.
[18] J. Yang, F.J. Zhang, X. Wang, D.S. He, G. Wu, Q.H. Yang, X. Hong, Y. Wu, Y.D. Li, Porous molybdenum phosphide nano-octahedrons derived from confined phosphorization in UIO-66 for efficient hydrogen evolution, Angew. Chem. Int. Edit. 55 (41) (2016) 12854–12858, https://doi.org/10.1002/anie.201604315.
[19] H. Lin, N. Liu, Z. Shi, Y. Guo, Y.i. Tang, Q. Gao, Cobalt-doping in molybdenum-carbide nanowires toward efficient electrocatalytic hydrogen evolution, Adv. Funct. Mater. 26 (31) (2016) 5590–5598, https://doi.org/10.1002/adfm.201600915.
[20] N. Yao, R. Meng, J. Su, Z. Fan, P. Zhao, W. Luo, Dual-phase engineering of MoN/Co_4N with tailored electronic structure for enhanced hydrogen evolution, Chem. Eng. J. (2020) 127757, https://doi.org/10.1016/j.cej.2020.127757.
[21] Y. Ma, M. Chen, H. Geng, H. Dong, P. Wu, X. Li, G. Guan, T. Wang, Synergistically tuning electronic structure of porous beta-Mo_2C spheres by Co doping and Mo-vacancies defect engineering for optimizing hydrogen evolution reaction activity, Adv. Funct. Mater. 30 (19) (2020), https://doi.org/10.1002/adfm.202000561.
[22] Y. Tang, W.Z. Li, L.X. Jiao, F. Li, Y.Y. Yang, X. Wang, W.B. Gao, R. Li, Mo_2C-Ni-modified nitrogen-doped carbon nanofiber toward efficient hydrogen evolution reaction, New J. Chem. 41 (21) (2017) 12956–12961, https://doi.org/10.1039/c7nj02611k.
[23] M. Li, Y. Zhu, H. Wang, C. Wang, N. Pinna, X. Lu, Ni strongly coupled with Mo_2C encapsulated in nitrogen-doped carbon nanofibers as robust bifunctional catalyst for overall water splitting, Adv. Energy Mater. 9 (10) (2019) 1803185, https://doi.org/10.1002/aenm.201803185.
[24] Z.Y. Yu, Y. Duan, M.-R. Gao, C.C. Lang, Y.-R. Zheng, S.-H. Yu, A one-dimensional porous carbon-supported Ni/Mo_2C dual catalyst for efficient water splitting, Chemical Science 8 (2) (2017) 968–973, https://doi.org/10.1039/c6sc03356c.
[25] Z.P. Wu, X.F. Lu, S.Q. Zang, X.W.(. Lou, Non-noble-metal-based electrocatalysts toward the oxygen evolution reaction, Adv. Funct. Mater. 30 (15) (2020) 1910274, https://doi.org/10.1002/adfm.201910274.
[26] N. Zhang, X. Feng, D. Rao, X. Deng, L. Cai, B. Qiu, R. Long, Y. Xiong, Y. Lu, Y. Chai, Lattice oxygen activation enabled by high-valence metal sites for enhanced water oxidation, Nat. Commun. 11 (1) (2020), https://doi.org/10.1038/s41467-020-17934-7.
[27] C. Wang, H. Yang, Y. Zhang, Q. Wang, NiFe alloy nanoparticles with hcp crystal structure stimulate superior oxygen evolution reaction electrocatalytic activity, Angew. Chem. Int. Edit. 58 (18) (2019) 6099–6103, https://doi.org/10.1002/anie.201902446.
[28] G. Zhang, J. Zeng, J. Yin, C. Zuo, P. Wen, H. Chen, Y. Qiu, Iron-facilitated surface reconstruction to in-situ generate nickel–iron oxyhydroxide on self-supported FeNi alloy fiber paper for efficient oxygen evolution reaction, Appl. Catal. B-Environ. 286 (2021) 119902, https://doi.org/10.1016/j.apcatb.2021.119902.
[29] M. Yao, N. Wang, W. Hu, S. Komarneni, Novel hydrothermal electrodeposition to fabricate mesoporous film of $Ni_{0.8}Fe_{0.2}$ nanosheets for high performance oxygen evolution reaction, Appl. Catal. B-Environ. 233 (2018) 226–233, https://doi.org/10.1016/j.apcatb.2018.04.009.
[30] D.Y. Chung, P.P. Lopes, P. Farinazzo Bergamo Dias Martins, H. He, T. Kawaguchi, P. Zapol, H. You, D. Tripkovic, D. Strmcnik, Y. Zhu, S. Seifert, S. Lee, V.R. Stamenkovic, N.M. Markovic, Dynamic stability of active sites in hydr(oxy)oxides for the oxygen evolution reaction (vol 5, pg 222, 2020), Nat. Energy 5(7) (2020) 550-550. https://doi.org/10.1038/s41560-020-0638-1.
[31] S.F. Zai, Y.T. Zhou, C.C. Yang, Q. Jiang, Al, Fe-codoped CoP nanoparticles anchored on reduced graphene oxide as bifunctional catalysts to enhance overall water splitting, Chem. Eng. J. (2020) 127856, https://doi.org/10.1016/j.cej.2020.127856.
[32] M.S. Burke, M.G. Kast, L. Trotochaud, A.M. Smith, S.W. Boettcher, Cobalt-Iron (Oxy)hydroxide oxygen evolution electrocatalysts: the role of structure and composition on activity, stability, and mechanism, J. Am. Chem. Soc. 137 (10) (2015) 3638–3648, https://doi.org/10.1021/jacs.5b00281.
[33] Q. Zhou, Y. Chen, G. Zhao, Y. Lin, Z. Yu, X. Xu, X. Wang, H.K. Liu, W. Sun, S. X. Dou, Active-site-enriched iron-doped nickel/cobalt hydroxide nanosheets for enhanced oxygen evolution reaction, ACS Catal. 8 (6) (2018) 5382–5390, https://doi.org/10.1021/acscatal.8b01332.
[34] R.Q. Yao, H. Shi, W.B. Wan, Z. Wen, X.Y. Lang, Q. Jiang, Flexible Co-Mo-N/Au electrodes with a hierarchical nanoporous architecture as highly efficient electrocatalysts for oxygen evolution reaction, Adv. Mater. 32 (10) (2020), https://doi.org/10.1002/adma.201907214.
[35] Y. Liu, X. Liang, L. Gu, Y. Zhang, G.D. Li, X. Zou, J.S. Chen, Corrosion engineering towards efficient oxygen evolution electrodes with stable catalytic activity for over 6000 hours, Nat. Commun. 9 (2018), https://doi.org/10.1038/s41467-018-05019-5.
[36] X. Zhang, Z. Zhu, X. Liang, F.X. Ma, J. Zhang, Y. Tan, Z. Pan, Y. Bo, C.M.L. Wu, Encapsulating dual-phased Mo_2C-WC nanocrystals into ultrathin carbon nanosheet assemblies for efficient electrocatalytic hydrogen evolution, Chem. Eng. J. 408 (2021), https://doi.org/10.1016/j.cej.2020.127270.
[37] Z. Shi, Y. Wang, H. Lin, H. Zhang, M. Shen, S. Xie, Y. Zhang, Q. Gao, Y. Tang, Porous nanoMoC@graphite shell derived from a MOFs-directed strategy: an efficient electrocatalyst for the hydrogen evolution reaction, J. Mater. Chem. A 4 (16) (2016) 6006–6013, https://doi.org/10.1039/c6ta01900e.
[38] H. Yan, Y. Xie, A. Wu, Z. Cai, L. Wang, C. Tian, X. Zhang, H. Fu, Anion-modulated HER and OER activities of 3D Ni-V-based interstitial compound heterojunctions for high-efficiency and stable overall water splitting, Adv. Mater. 31 (23) (2019), https://doi.org/10.1002/adma.201901174.
[39] S.P. Wang, J. Wang, M.L. Zhu, X.B. Bao, B.Y. Xiao, D.F. Su, H.R. Li, Y. Wang, Molybdenum-carbide-modified nitrogen-doped carbon vesicle encapsulating nickel nanoparticles: a highly efficient, low-cost catalyst for hydrogen evolution reaction, J. Am. Chem. Soc. 137 (50) (2015) 15753–15759, https://doi.org/10.1021/jacs.5b07924.
[40] K. Xiong, L. Li, L. Zhang, W. Ding, L. Peng, Y. Wang, S. Chen, S. Tan, Z. Wei, Ni-doped Mo_2C nanowires supported on Ni foam as a binder-free electrode for enhancing the hydrogen evolution performance, J. Mater. Chem. A 3 (5) (2015) 1863–1867, https://doi.org/10.1039/c4ta05686h.
[41] Z. Liu, S. Zhou, S. Xue, Z. Guo, J. Li, K. Qu, W. Cai, Heterointerface-rich Mo_2C/MoO_2 porous nanorod enables superior alkaline hydrogen evolution, Chem. Eng. J. (2020) 127807, https://doi.org/10.1016/j.cej.2020.127807.
[42] H. Tabassum, W. Guo, W. Meng, A. Mahmood, R. Zhao, Q. Wang, R. Zou, Metal-organic frameworks derived cobalt phosphide architecture encapsulated into B/N Co-doped graphene nanotubes for all pH value electrochemical hydrogen evolution, Adv. Energy Mater. 7 (9) (2017), https://doi.org/10.1002/aenm.201601671.
[43] B. Zhang, J. Wang, J. Liu, L. Zhang, H. Wan, L. Miao, J. Jiang, Dual-descriptor tailoring: the hydroxyl adsorption energy-dependent hydrogen evolution kinetics of high-valance state doped Ni_3N in alkaline media, ACS Catal. 9 (10) (2019) 9332–9338, https://doi.org/10.1021/acscatal.9b01637.
[44] L. Mi, J. Yu, F. He, L. Jiang, Y. Wu, L. Yang, X. Han, Y. Li, A. Liu, W. Wei, Y. Zhang, Y. Tian, S. Liu, L. Jiang, Boosting gas involved reactions at nanochannel reactor with joint gas-solid-liquid interfaces and controlled wettability, J. Am. Chem. Soc. 139 (30) (2017) 10441–10446, https://doi.org/10.1021/jacs.7b05249.
[45] R.A. Mir, O.P. Pandey, Influence of graphitic/amorphous coated carbon on HER activity of low temperature synthesized β-Mo_2C@C nanocomposites, Chem. Eng. J. 348 (2018) 1037–1048, https://doi.org/10.1016/j.cej.2018.05.041.
[46] L. Trotochaud, S.L. Young, J.K. Ranney, S.W. Boettcher, Nickel-iron oxyhydroxide oxygen-evolution electrocatalysts: the role of intentional and incidental iron incorporation, J. Am. Chem. Soc. 136 (18) (2014) 6744–6753, https://doi.org/10.1021/ja502379c.
[47] X. Han, X. Wu, Y. Deng, J. Liu, J. Lu, C. Zhong, W. Hu, Ultrafine Pt nanoparticle-decorated pyrite-type CoS_2 nanosheet arrays coated on carbon cloth as a bifunctional electrode for overall water splitting, Adv. Energy Mater. 8 (24) (2018), https://doi.org/10.1002/aenm.201800935.
[48] J. Yu, Q.Q. Li, Y. Li, C.Y. Xu, L. Zhen, V.P. Dravid, J.S. Wu, Ternary metal phosphide with triple-layered structure as a low-cost and efficient electrocatalyst for bifunctional water splitting, Adv. Funct. Mater. 26 (42) (2016) 7644–7651, https://doi.org/10.1002/adfm.201603727.
[49] J. Zhang, T. Wang, D. Pohl, B. Rellinghaus, R. Dong, S. Liu, X. Zhuang, X. Feng, Interface engineering of MoS_2/Ni_3S_2 heterostructures for highly enhanced electrochemical overall-water-splitting activity, Angew. Chem. Int. Edit. 55 (23) (2016) 6702–6707, https://doi.org/10.1002/anie.201602237.
[50] T. Ouyang, X.T. Wang, X.Q. Mai, A.N. Chen, Z.Y. Tang, Z.Q. Liu, Coupling magnetic single-crystal $Co_2Mo_3O_8$ with ultrathin nitrogen-rich carbon layer for oxygen evolution reaction, Angew. Chem. Int. Edit. 59 (29) (2020) 11948–11957, https://doi.org/10.1002/anie.202004533.
[51] S. Liu, J. Zhu, M. Sun, Z. Ma, K. Hu, T. Nakajima, X. Liu, P. Schmuki, L. Wang, Promoting the hydrogen evolution reaction through oxygen vacancies and phase transformation engineering on layered double hydroxide nanosheets, J. Mater. Chem. A 8 (5) (2020) 2490–2497, https://doi.org/10.1039/c9ta12768b.
[52] M. Yang, T. Feng, Y. Chen, J. Liu, X. Zhao, B. Yang, Synchronously integration of Co, Fe dual-metal doping in Ru@C and CDs for boosted water splitting performances in alkaline media, Appl. Catal. B-Environ. 267 (2020), https://doi.org/10.1016/j.apcatb.2020.118657.
[53] X. Yu, M. Zhang, Y. Tong, C. Li, G. Shi, A large-scale graphene-bimetal film electrode with an ultrahigh mass catalytic activity for durable water splitting, Adv. Energy Mater. 8 (21) (2018), https://doi.org/10.1002/aenm.201800403.
[54] H. Huang, S. Zhou, C. Yu, H. Huang, J. Zhao, L. Dai, J. Qiu, Rapid and energy-efficient microwave pyrolysis for high-yield production of highly-active bifunctional electrocatalysts for water splitting, Energy Environ. Sci. 13 (2) (2020) 545–553, https://doi.org/10.1039/c9ee03273h.
[55] H. Sun, J.M. Yang, J.G. Li, Z. Li, X. Ao, Y.Z. Liu, Y. Zhang, Y. Li, C. Wang, J. Tang, Synergistic coupling of NiTe nanoarrays with RuO_2 and NiFe-LDH layers for high-efficiency electrochemical-/photovoltage-driven overall water splitting, Appl. Catal. B-Environ. 272 (2020), https://doi.org/10.1016/j.apcatb.2020.118988.